Geophysical Research Letters

RESEARCH LETTER
10.1029/2023GL104067

Surface-Volume Scaling Controlled by Dissolution Regimes in a Multiphase Flow Environment

Chen-Xing Zhou[1,2], Ran Hu[1,2], Hang Deng[3], Bowen Ling[4,5], Zhibing Yang[1,2], and Yi-Feng Chen[1,2]

[1]State Key Laboratory of Water Resources Engineering and Management, Wuhan University, Wuhan, China, [2]Key Laboratory of Rock Mechanics in Hydraulic Structural Engineering of the Ministry of Education, Wuhan University, Wuhan, China, [3]Department of Energy & Resources Engineering, College of Engineering, Peking University, Beijing, China, [4]Institute of Mechanics, Chinese Academy of Sciences, Beijing, China, [5]School of Engineering Science, University of Chinese Academy of Sciences, Beijing, China

Abstract Fluid-rock dissolution occurs ubiquitously in geological systems. Surface-volume scaling is central to predicting overall dissolution rate R involved in modeling dissolution processes. Previous works focused on single-phase environments but overlooked the multiphase-flow effect. Here, through limestone-based microfluidics experiments, we establish a fundamental link between dissolution regimes and scaling laws. In regime I (uniform), the scaling is consistent with classic law, and a satisfactory prediction of R can be obtained. However, the scaling for regime II (localized) deviates significantly from classic law. The underlying mechanism is that the reaction-induced gas phase forms a layer, acting as a barrier that hinders contact between the acid and rock. Consequently, the error between measurement and prediction continuously amplifies as dissolution proceeds; the predictability is poor. We propose a theoretical model that describes the regime transition, exhibiting excellent agreement with experimental results. This work offers guidance on the usage of scaling law in multiphase flow environments.

Plain Language Summary Fluid-rock dissolution is ubiquitous in natural and engineered systems, including karst formation, geological carbon sequestration, and acid stimulation. Recent developed method for CO_2 sequestration relies on mineralization, which transforms CO_2 into carbonate minerals through geochemical reactions involving dissolution. The precise modeling of dissolution processes at the continuum-scale is dependent on the estimation of the overall dissolution rate using surface-volume scaling laws. This important scaling law is always established in a single-phase system. Here, through limestone-based microfluidics experiments, we find that the scaling is significantly affected by the dissolution regime in a multiphase flow environment. When the injection rate is lower, and the geometry is more homogeneous, the dissolution regime adheres to classic law. On the other hand, when the flow is stronger and the heterogeneity exhibits, the dissolution scaling significantly diverges. Our discovery indicates that a layer of CO_2 gas attaches to the uneven surface, causing a shielding effect on the dissolution and resulting in a notable deviation. Through establishing a theoretical model for the regime transition, this work offers guidance on the usage of scaling law across various dissolution scenarios. The newly developed scaling can enhance dissolution modeling precision in multiphase flow-dissolution systems such as geologic carbon sequestration.

Key Points:

- We observe two regimes, and the scaling in regime II deviates significantly from classic law, with a poor predictability of dissolution rate
- We identify a barrier effect in real rock samples that inhibits the contact of acid and rock for the deviation of scaling in regime II
- We propose a theoretical model for regime transition that offers guidance on the usage of scaling law in multiphase environments

Supporting Information:

Supporting Information may be found in the online version of this article.

Correspondence to:

R. Hu and B. Ling,
whuran@whu.edu.cn;
lingbowen@imech.ac.cn

Citation:

Zhou, C.-X., Hu, R., Deng, H., Ling, B., Yang, Z., & Chen, Y.-F. (2023). Surface-volume scaling controlled by dissolution regimes in a multiphase flow environment. *Geophysical Research Letters*, *50*, e2023GL104067. https://doi.org/10.1029/2023GL104067

Received 11 APR 2023
Accepted 4 SEP 2023

Author Contributions:

Conceptualization: Ran Hu, Bowen Ling
Funding acquisition: Ran Hu, Bowen Ling, Zhibing Yang, Yi-Feng Chen
Investigation: Chen-Xing Zhou, Ran Hu, Hang Deng, Bowen Ling
Methodology: Chen-Xing Zhou, Ran Hu, Hang Deng, Bowen Ling
Project Administration: Ran Hu, Zhibing Yang, Yi-Feng Chen
Resources: Ran Hu
Software: Chen-Xing Zhou
Supervision: Ran Hu
Validation: Chen-Xing Zhou, Ran Hu
Visualization: Chen-Xing Zhou

1. Introduction

Fluid-rock dissolution is ubiquitous in natural and engineered systems, including geological carbon sequestration (GCS) (Celia, 2017; Fitts & Peters, 2013; Steefel et al., 2013; T. Xu et al., 2022; L. Zhang et al., 2022), karst formation (Hanna & Rajaram, 1998; Romanov et al., 2003), acid stimulation (Kiani et al., 2021; Middleton et al., 2017; Panga et al., 2005), mobilization of hazardous metals and metalloids (Deng et al., 2020; C. Wang et al., 2015). When the reactive fluid is in contact with rock, chemical reactions at fluid-rock interfaces will alter the pore structure and significantly impact the geochemical and geophysical properties (Hu et al., 2021, 2023; T. Wang et al., 2022). For example, the caprock security at a GCS site is primarily influenced by the dissolution of the formation, which is determined by rock mineralogy (Al-Khulaifi et al., 2019), structure heterogeneity (Deng et al., 2018; Roded et al., 2021; Y. Zhang et al., 2022; Zhou et al., 2022), and length scale (L. Li et al., 2008).

In the aforementioned applications, reactive transport models are expected to provide predictions of, for instance, the overall reaction progression of formation, reaction hotspots, and formation transmissivity change

Writing – original draft: Chen-Xing Zhou, Ran Hu
Writing – review & editing: Chen-Xing Zhou, Ran Hu, Hang Deng, Bowen Ling

due to reaction. Continuum-scale transport models demonstrated the potential in handling dissolution problems at large-scale application scenarios (Esteves et al., 2022; Steefel & Maher, 2009; Steefel et al., 2015; Wen & Li, 2017). Despite this, there is a significant disparity of several orders of magnitude between laboratory measurements and predictions made by reactive transport models regarding reaction rate (Le Traon et al., 2021; Liu et al., 2022). Previous investigations have recognized that the key limitation comes from the parameters (e.g., reaction rate constant, specific surface area, etc.) used in the continuum-scale model (Beckingham et al., 2016; Deng, Molins, et al., 2018; L. Li et al., 2008; Qin & Beckingham, 2021). These parameters require the knowledge of the pore-scale reactive transport process and are difficult to be determined by continuum-scale experiments solely. Thus, a comprehensive understanding of the pore-scale reactive transport mechanism is crucial in providing a more accurate estimation of the parameters used in the large-scale model and further enhancing the predictivity of the continuum-scale model (Seigneur et al., 2019; Steefel et al., 2015; Yoon et al., 2012).

Accurate estimation of the reaction rates is a prerequisite for the successful simulation of continuum-scale reactive transport. Reactive transport code, such as CrunchFlow ®, estimates the reaction rate R with

$$R = Akf_e \tag{1}$$

where A is the reactive surface area, k is the reaction rate constant, and f_e is a function of Gibbs free energy or the thermodynamic driving force, which is related to the concentration of reactants (Beckingham et al., 2016; Lasaga, 1984; Ling et al., 2022). Since the reaction rate constant and thermodynamic properties of mineral dissolution reactions are generally well understood, the principal uncertainties in modeling mineral reaction rates come from the estimation of mineral reactive surface area A (Beckingham et al., 2017; Qin & Beckingham, 2021). This reactive surface area A is usually estimated using a classic relationship:

$$A(t) = A^i \left(\frac{\Phi_m(t)}{\Phi_m^i} \right)^{2/3} \left(\frac{\Phi(t)}{\Phi^i} \right)^{2/3} \tag{2}$$

where Φ is the porosity and Φ_m is the individual mineral volume fraction (Ling et al., 2022; Qin & Beckingham, 2021; Seigneur et al., 2019; Steefel & Lichtner, 1998). The superscript "i" refers to the corresponding quantity evaluated at $t = 0$. However, this equation is derived under the assumption that mineral grain is dissolved uniformly and the predictability of the scaling law under complex systems needs to be further studied (Noiriel & Daval, 2017; Seigneur et al., 2019; Steefel & Lichtner, 1998).

The dissolution process in a multiphase environment is prevalent in subsurface systems due to the emergence of the gas phase resulting from direct gas injection, chemical reactions, depressurization, or heating (Holocher et al., 2003; Ott & Oedai, 2015; Song et al., 2018; Yortsos & Stubos, 2001; Yu et al., 2023; Zuo et al., 2013). Reactive transport models mainly deal with the dissolution process under the single-phase flow condition (Deng et al., 2018; Molins et al., 2021; Noiriel & Soulaine, 2021; Steefel et al., 2015). Previous works have shown significant effects of multiphase flow on dissolution dynamics (P. Li et al., 2022; Soulaine et al., 2018; Thompson & Gdanskl, 1993; J. Xu & Balhoff, 2022). Soulaine et al. (2018) develop a pore-scale model to reproduce the generation of CO_2 bubbles during the dissolution process of calcite, revealing that bubbles prevent the emergence of the wormhole and limit the overall dissolution rate in porous media. P. Li et al. (2022) also simulated the dissolution processes under multiphase flow conditions, showing that the suppression of the overall dissolution rate is due to the occupation of the reactive surface area by non-reactive bubbles and the limited transport by the recirculation zones in troughs. Jiménez-Martínez et al. (2020) showed that multiphase flow significantly modifies the competition between flow and reaction, and the local dissolution rate tends to be uniform in the flow domain. These works highlight the key role of multiphase flow in dissolving confined geometry. However, how the pore-scale multiphase flow controls the interface-volume relationship (Equation 2) used in the continuum-scale reactive transport modeling is not well understood.

Here, we aim to elucidate how multiphase flow affects reactive transport via interface-volume relationship quantification. By conducting experimental observations and quantification, we correlate the dissolution regimes with surface-volume scaling laws and propose a theoretical model for the regime transition. Our findings reveal that the classic scaling's suitability is dependent on the dissolution regimes. Our research bridges the gap between pore-scale dissolution dynamics and the overall dissolution rate prediction in a multiphase flow system.

2. Materials and Methods

We perform multiphase flow-through dissolution experiments in the microfluidic-based visualization system (Figure S1 in Supporting Information S1). We fabricate soluble microfluidics using rectangular limestone slices (the thickness is 200 μm), as shown in Figures S2 and S3 in Supporting Information S1. To conduct a dissolution experiment, we saturate the microfluidics with deionized (DI) water. Then the HCl solution (pH ranging from 1 to 4, Codow Standard titration solution) is injected into the flow cell by a syringe pump (PhD Ultra 70-3007, Harvard Apparatus) with constant flow rates. To improve the differentiation between the liquid and gas phases (Figure S1d in Supporting Information S1), a fluorescent dye is added to the acid solution (0.1 mg/L, FLUORESCENCE Super Fluor 488). As the acidic solution is in contact with the carbonate rock slices, dissolution occurs, and the CO_2 gas phase forms expressed as

$$CaCO_3(s) + 2HCl(aq) = CaCl_2(s) + CO_2(g) + H_2O(aq)$$

The multiphase flow-dissolution process is recorded by the fluorescent microscopy visualization techniques (ZEISS AXIO Observer) coupled with a high-speed CMOS camera (Axiocam 305 color) (Figure S1d in Supporting Information S1). Through image processing (Figure S4 in Supporting Information S1), we calculate the solid-fluid interfaces $A(t)$, the fracture volume $\Phi(t)$, and the overall dissolution rate during dissolution.

We employ the classic Péclet number Pe and Damkohler number Da_{II} to quantify the interplay among advection, diffusion, and reaction, namely $Pe = vd_0/D_m$, $Da_{\mathrm{II}} = kd_0/D_m$, where v is the average velocity, $v = Q/[(2d_1 + d_2)h_0]$; $d_0 = 200$ μm is the width; D_m is the molecular diffusion coefficient, $D_m = 2 \times 10^{-9}$ m^2/s (Panga et al., 2005); k is the reaction rate constant of limestone depending on pH. The values of reaction rate constant are $k = 1 \times 10^{-6}$ m/s, 1×10^{-7} m/s, 1×10^{-8} m/s and 1×10^{-9} m/s for pH = 1, pH = 2, pH = 3 and pH = 4, respectively (Alarji et al., 2022). We conducted a total of 27 experiments, varying the flow rate Q from 0.24 to 24 μL/min, the pH from 1 to 4, and the geometry parameter λ ($\lambda = d_2/d_1$) from 0.26 to 2.6. The experimental conditions and the related parameters are listed in Table S1 in Supporting Information S1.

3. Results and Discussion

3.1. Observation of Dissolution Regimes

From Figure 1, we observe two distinct dissolution regimes forming in the multiphase flow environment, namely regime I (Figure 1c) and regime II (Figure 1b). In regime I, the limestone is mainly dissolved in the perpendicular (vertical) channels (the initial aperture is d_1), and the aperture of these two channels increases significantly. On the contrary, in regime II, the dissolution mainly occurs in the longitudinal (horizontal) channel (the initial aperture is d_2), leading to a localized dissolution channel in the flow direction. The typical dissolution processes of rock surfaces with injected time are shown in Figures 1d and 1e. The emergence and transformation of the two different dissolution regimes are influenced by the interplay between reaction and multiphase flow.

To understand the role of multiphase flow in dissolving rough fractures, we also present the fluid phase distribution, namely the HCl solution (fluid) and CO_2 (gas), in Figure 1a. For the lowest flow rate considered ($Q = 0.24$ μL/min, Figure $1a_9$–$1a_{12}$), regime I forms for all λ. In general, due to the lower flow resistance, the HCl solution is anticipated to flow mainly through the channels with a higher permeability. In the case of large λ ($\lambda > 1$) that the longitudinal channel has the larger permeability, HCl solution primarily flows through the longitudinal channel, leading to preferential dissolution. However, our experiments (Figures $1a_9$–$1a_{12}$) indicate that the dissolution primarily takes place in the perpendicular channels, regardless of the λ involved. This inconsistency highlights the substantial impact of multiphase flow on shaping the flow channels. In a multiphase environment, two factors dictate the infiltration of HCl solution into the channels: pressure drop and flow resistance from CO_2 bubbles. The CO_2 bubbles, resulting from the HCl and limestone reaction, create a non-wetting phase that occupies the longitudinal channels, leading to additional flow resistance and hindering HCl solution infiltration.

The above discussion indicates that in the case of the lowest flow rate ($Q = 0.24$ μL/min, Figure $1a_9$–$1a_{12}$), the flow resistance created by the CO_2 bubbles exceeds the pressure drop generated by the injected flow. This indicates that the multiphase flow resistance dominates the flow-reaction system, outweighing the advection from the flow rate. As a result, the longitudinal channel cannot be invaded by the HCl solution, while the perpendicular channels are able to be invaded, leading to the formation of regime I. As Q and λ values increase, the pressure

10.1029/2023GL104067

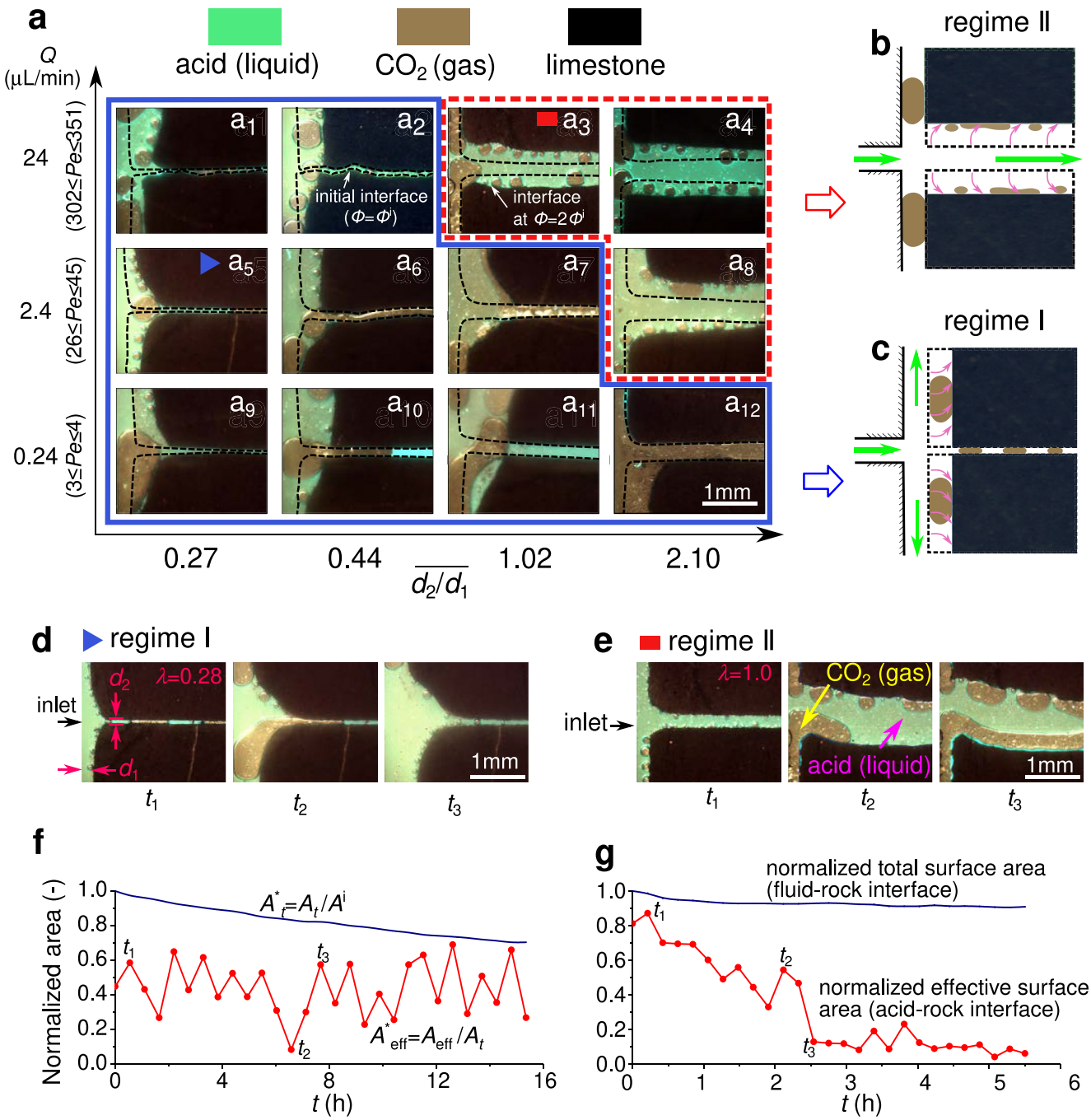

Figure 1. Experimental phase diagram of dissolution regimes for pH = 1. (a) Dissolution morphologies at the time of $\Phi = 2\Phi^i$ under three flow rates (Q) and four geometry parameters ($\lambda = d_2/d_1$) conditions. The Pe number (or the flow rate Q) increases from the bottom to the top. The initial solid-fluid interfaces are denoted as black dashed lines. Hydrochloric acid (HCl) solution, carbonate slice, and CO_2 phase (gas) are shown as green, dark, and light brown, respectively. Two distinct dissolution regimes are observed, denoted as regime I (c) and regime II (b). In regime I (uniform), dissolution mainly occurs in the two perpendicular (vertical) channels (c), whereas the dissolution of limestone occurs along the longitudinal (horizontal) channel in regime II (b). (d, e) Typical dissolution processes with injected time for the two regimes (Movies S1 and S2). The evolution of the rock surfaces with the injected volume for all experimental conditions is shown in Figure S5 in Supporting Information S1. The variations of the normalized total surface area (fluid-rock interface) and the normalized effective area (acid-rock interface) are presented in (f) and (g) for regime I (d) and regime II (e). The reproducibility of the experimental results is shown in Figure S6 in Supporting Information S1. The experimental phase diagrams of dissolution regimes for pH = 2, pH = 3, and pH = 4 are shown in Figure S10 in Supporting Information S1.

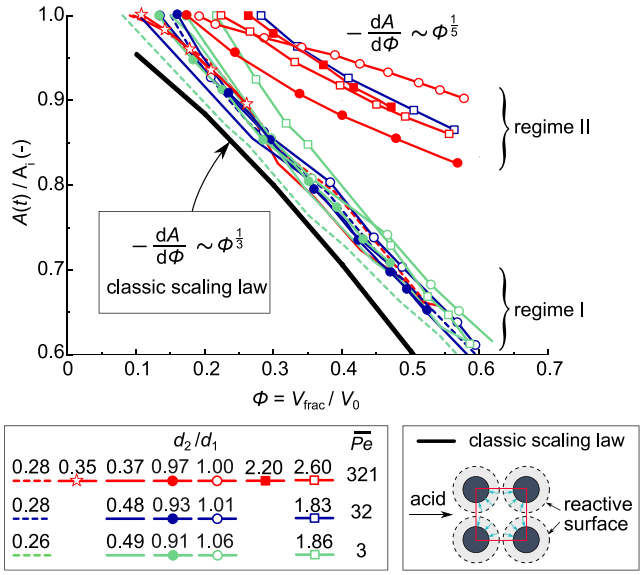

Figure 2. The fundamental link between dissolution regimes and scaling laws. The scaling relationship between $A(t)$ and $\Phi(t)$ depends on dissolution regimes. The scaling relationship of regime I is consistent with classical law, namely $-dA/d\Phi \sim \Phi^{1/3}$ (Text S1 in Supporting Information S1). The classic scaling law that assumes uniform dissolution of mineral grains is also shown for comparison purposes. In regime II, the scaling relationship deviates from the classical law, with the power index decreasing from 1/3 (classic law or regime I) to 1/5 (regime II). The slope of the A-ϕ scaling curves remains relatively constant within the range of porosity ($0.1 \leq \phi \leq 0.6$) for both two regimes, with -0.98 ± 0.09 for regime I, and -0.53 ± 0.10 for regime II (Figure S11 in Supporting Information S1). Thus, the power-law scaling curves exhibit straight lines in linear scale plots.

drop gradually rises while the flow resistance decreases. When the two effects become comparable, a transition of the dissolution regimes occurs. As shown in Figures $1a_5$–a_8 ($Q = 2.4$ μL/min), the dissolution exhibits regime I for $\lambda \leq 1.02$, and it shifts to regime II as λ increases up to 2.10. In regime II (a larger λ), the flow resistance from CO_2 bubbles is insufficient to prevent the HCl solution from invading the longitudinal channel. The majority of injected flow passes through the longitudinal channel, and the dissolution is therein localized (Jiménez-Martínez et al., 2020; Roded et al., 2020).

As Q further increases up to $Q = 24$ μL/min (Figures $1a_1$–$1a_4$), the critical λ corresponding to regime transition decreases (a point between Figures $1a_2$ and $1a_3$). As the pressure drop rises, a greater flow resistance (smaller λ) is required to counteract this drop. In a word, our experimental findings and analysis demonstrate that multiphase flow plays a crucial role in shaping the formation and transformation of dissolution regimes by inducing extra flow resistance.

3.2. Scaling Laws Controlled by Dissolution Regimes

As indicated in the Introduction, surface-volume scaling is a central relationship to estimating the overall dissolution rate involved in a continuum-scale transport model. In this subsection, we will study how dissolution regimes (quantified in Figure 1) affect this scaling relationship. We calculate the evolution of $A(t)$ and fracture volume $\Phi(t)$ and present the results in Figure 2. We also present the classic law obtained in single-phase flow system for comparison. Interestingly, for the first time, we find a fundamental link between dissolution regimes (Figure 1) and surface-volume scaling laws. In regime I, all of the experimental data is consistent with the classic scaling law with the same exponent 1/3:

$$-\frac{dA}{d\Phi} \sim \Phi^{1/3} \tag{3}$$

However, the surface-volume scaling in regime II deviates significantly from the classic law, with the exponent being 1/5:

$$-\frac{dA}{d\Phi} \sim \Phi^{1/5} \tag{4}$$

The detailed derivation of the classic scaling law (Equation 3) is given in Text S1 in Supporting Information S1. It is shown in Figure 1 that multiphase flow significantly affects the formation and transition of the dissolution patterns through the additional flow resistance induced by the CO_2 phase. In addition to the experimental observations and analyses, there are still unanswered mechanistic questions, such as why the scaling law in regime I in multiphase-flow systems is consistent with the classic law in single-phase flow system, and why the scaling law in regime II deviates significantly from the classic law.

We note that the underlying assumption of the classic scaling law under a single-phase flow environment is that rock samples have a high carbonate content and the mineral grains are uniformly dissolved (Ling et al., 2022; Noiriel & Daval, 2017; Seigneur et al., 2019; Steefel & Lichtner, 1998; Steefel et al., 2015), as shown in Figure 2. In realistic application scenarios, the presence of complex multiphase hydrodynamics, mineralogy, and pore geometry weakens the uniformity assumption and leads the classic scaling law to deviation (Ling et al., 2022; Noiriel & Daval, 2017). Our study reveals that despite the significant influence of multiphase flow on the dissolution processes, the dissolution dynamics of regime I exhibit a similar morphology to that of the single-phase flow environment. The materials used in this work have a high carbonate content (92.87%, Figure S2 in Supporting Information S1), driving the experimental data to be consistent with the classic law. We acknowledge that bubbles are expected to appear in both perpendicular and horizontal channels. The mobility of the generated bubbles differs due to flow heterogeneity, that is, whether the channel is parallel or perpendicular to the incoming flow,

and geometrical anisotropy, that is, differences in channel aperture. This disparity in mobility causes the bubbles to either be flushed away or merge, ultimately resulting in a deviation of the dissolution pattern toward the two observed regimes. Specifically, regime I is characterized by limestone dissolution primarily occurring in the perpendicular (vertical) channels, resulting in a significant increase in aperture size in these channels. In this case, the reaction-induced CO_2 bubbles would be flushed away perpendicular to the incoming flow. The effective area, that is, the acid-rock interface area, fluctuates as the dissolution proceeds, as evidenced by Figure 1e. However, regime II is characterized by dissolution predominantly occurring in the longitudinal (horizontal) channel. It causes the merged bubbles to shrink by strong incoming flow, eventually forming a CO_2 film as a *barrier* (Figure S7 in Supporting Information S1). Such an effect leads to the fact that the acid-rock interface area gradually decreases as dissolution progresses, as shown in Figure 1g. Therefore, the dissolution dynamics in regime II break the uniform dissolution assumption of the classic scaling law, leading to a significant deviation.

3.3. Model Predictability Controlled by Dissolution Regimes

As previously indicated, the dissolution regime significantly affects the scaling relationship of the reactive surface area and thus has a direct impact on the overall reaction rate. To investigate how the dissolution regimes control the applicability and predictability of the scaling laws used in the reactive transport model, we compare the predicted reaction rate, $R_{t,\mathrm{pre}}$, with the measured reaction rate $R_{t,\mathrm{exp}}$, for the two dissolution regimes. The measured rate, $R_{t,\mathrm{exp}}$, can be obtained via post-processing of the fluorescent images (Figure S4 in Supporting Information S1):

$$R_{t,\mathrm{exp}} = \frac{\Delta V_t}{\Delta t} \tag{5}$$

where ΔV_t is the dissolved volume of the limestone within the time interval Δt (Figure S4 in Supporting Information S1).

The predicted rate, $R_{t,\mathrm{pre}}$, can be obtained by substituting Equation 2 into Equation 1:

$$R_{t,\mathrm{pre}} = A(t) k f_{\mathrm{e}} \tag{6}$$

where $k = 1 \times 10^{-6}$ m/s for pH = 1 (Alarji et al., 2022); f_{e} can be considered as the inflow concentration C_{in} under acidic pH, $f_{\mathrm{e}} = C_{\mathrm{in}}$ (Noiriel et al., 2007; Panga et al., 2005); $A(t)$ is the using the measured reactive surface area A in Figure 2.

To quantify the applicability and predictability of the scaling laws controlled by dissolution regimes, we introduce a correction factor C_{f} and its trend of the variation k_{avg}:

$$C_{\mathrm{f}} = \frac{R_{t,\mathrm{pre}}}{R_{t,\mathrm{exp}}} \tag{7a}$$

$$k_{\mathrm{avg}} = \frac{1}{n} \sum_{i=1}^{n} \frac{\Delta C_{\mathrm{f},i}}{\Delta t_i} \tag{7b}$$

where k_{avg} is the average slope of C_{f} curve to represent the trend of the variation of C_{f}; $\Delta C_{\mathrm{f},i}$ is the variation of C_{f} during the time interval Δt_i; n is the total number of time intervals. A larger value of k_{avg} denotes the increases of C_{f} with a higher growth rate; a lower value of k_{avg} shows that C_{f} fluctuates.

Figure 3a presents the variations of C_{f} during dissolution, showing that there is one order of magnitude difference between the predicted and measured reaction rate. This discrepancy is expected because some factors cannot be considered using Equation 1, including the transport limitation depending on the scale (L. Li et al., 2008), precipitation-induced passivation (Noiriel et al., 2007), and surface area accessibility (Beckingham et al., 2017). Here, we focus on the trend of the variation of C_{f} affected by dissolution regimes during multiphase reactive flow. Qualitatively, the arrows stand for the trend of C_{f} are shown in Figure 3. We observe that in dissolution regime I, the correction factor C_{f} fluctuates around a stable value (Figures $3a_1$–$3a_9$), indicating that a satisfactory prediction for the reaction rate can be approached by shifting a constant. In other words, the classic model can be applied by introducing a constant correction factor C_{f}. However, in dissolution regime II, such correction factor C_{f} continuously increases as dissolution proceeds (Figures $3b_1$–$3b_3$), indicating that the difference between $R_{\mathrm{t,pre}}$ and $R_{\mathrm{t,exp}}$ amplifies. It thus implies that the classic model fails to estimate the dissolution rate in the regime II.

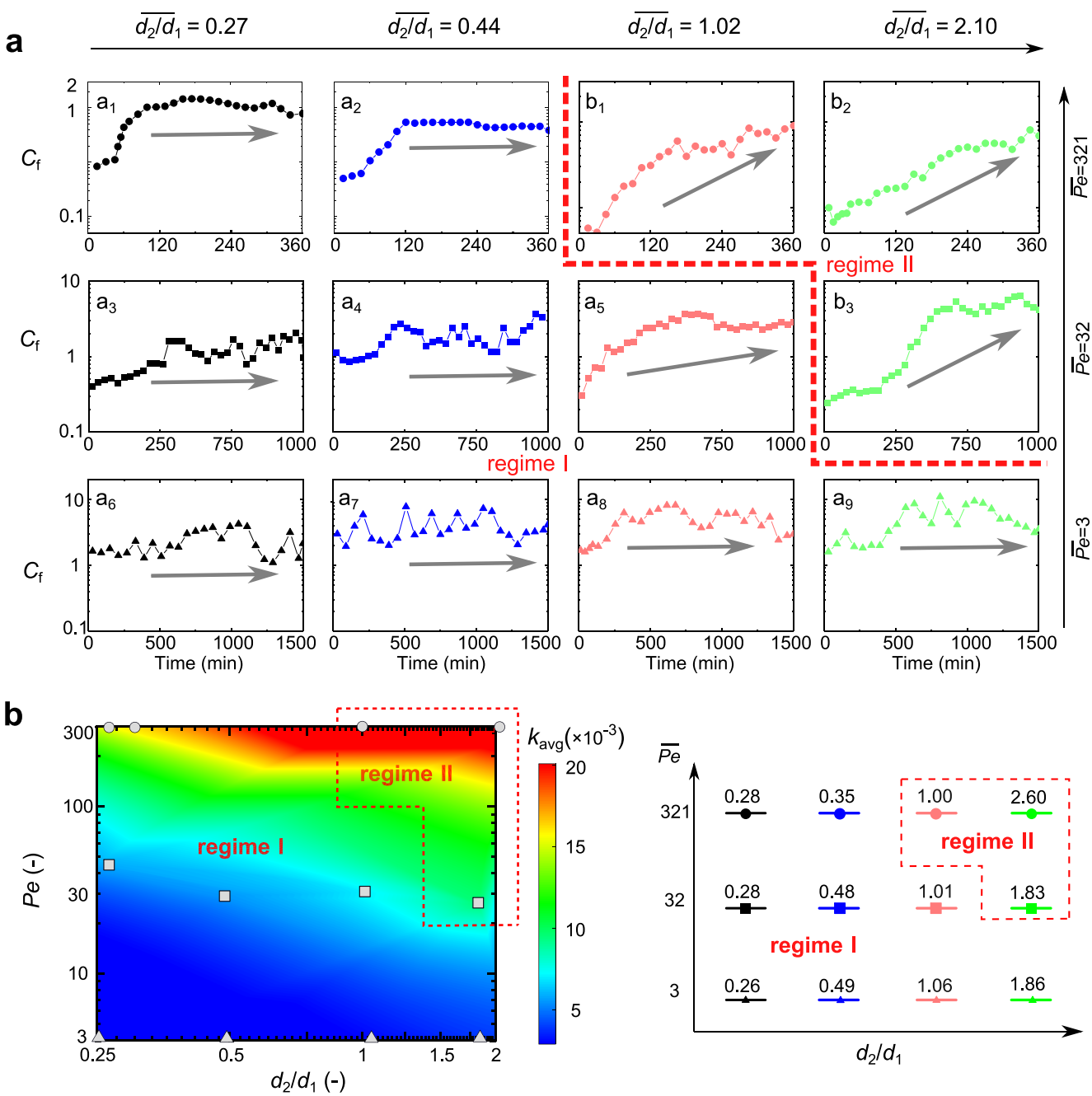

Figure 3. Model predictability controlled by dissolution regimes. (a) Variations of correction factor C_f for all experimental conditions. C_f is ratio of the predicted to the measured reaction rates. In regime I, the correction factor C_f fluctuates around a stable value. In regime II, C_f continuously increases, and the difference between the predicted and measured reaction rates amplifies. The classic model fails to estimate the dissolution rate in this regime. (b) Contour plot of the average slope of C_f (k_{avg}). k_{avg} is used to quantify the trend of C_f affected by dissolution regimes. As the dissolution regime shifts from I to II, C_f increases, indicating that the predictability decreases.

The dependence of the applicability and predictability of the scaling laws on the regimes can be further indicated by the contour plot of k_{avg} (Figure 3b). From Figure 3b, we observe that as the dissolution regime shifts from I to II, the average slope increases, implying that C_f increases with a higher growth rate in regime II. Consistent with Figure 3a, it evidences that the contour plot of k_{avg} overlaps with the phase diagram of dissolution regimes in Figure 1. As dissolution regime I occurs, the dissolution rate can be predicted by modifying the classic reaction rate model with a constant C_f due to its fluctuation with the normalized effective area (Figure 1f and Figure S8a in Supporting Information S1). However, in regime II, C_f cannot reach a stable plateau, and the error of reaction

rate predicted by the model (Equation 1) amplifies as the dissolution processes because the dissolution rate is suppressed by the *barrier* effect (Figure 1g and Figure S8b in Supporting Information S1). Although this shifting method using the correction factor C_f is practiced in some previous studies (Beckingham et al., 2016; Hyman et al., 2022), our work quantifies its predictability controlled by dissolution regimes in a multiphase flow environment for the first time.

3.4. Theoretical Model for the Regime Transition

As previously indicated in Section 3.1, regime I is distinguished by the dissolution of limestone in channels perpendicular to the flow direction, whereas in regime II, transport and dissolution take place primarily in the longitudinal channel. We propose a theoretical model for the regime transition to generalize our experimental findings under various pH (or Da_{II}) conditions. The regime to which the dissolution dynamic belongs is determined by whether the bubble in the longitudinal channel moves or not. Therefore, we consider the critical state when a bubble forms in the longitudinal channel (Figure S9 in Supporting Information S1). Under such a state, the fluid flow in this channel is controlled by the interplay between driving force and resistance. For the multiphase flow in wetting media (imbibition), the driving force is from two components (Hu et al., 2018, 2019), including the viscous pressure P_{vis} along the characteristic length δx and capillary pressure P_{cap} on the water-CO_2 interface. The resistance P_{gas} is from CO_2 bubbles generated during a unit time period Δt. The fluid flow behavior in the longitudinal channel can be described as:

$$\frac{Q_{in}}{A_{in}} = \frac{K}{\mu L}\left(P_{vis} + P_{cap} - P_{gas}\right) \tag{8}$$

where Q_{in} and A_{in} are the flow rate and area of the inlet; K is the effective permeability of the channel; μ is viscosity and L is the characteristic length scale in the longitudinal direction.

Substituting $Pe = Q_{in}/[D_m(2d_1 + d_2)]$, $Da_{II} = kd_0/D_m$ and $\lambda = d_2/d_1$ into Equation 8, we establish a theoretical model for the regime transition (Text S2 in Supporting Information S1):

$$Pe_{cr} = \frac{1}{\lambda(\lambda + 2 - \varepsilon)} \frac{\beta\sigma - 2\Psi(Da_{II})}{C_0} \tag{9a}$$

with

$$\Psi(Da_{II}) = Da_{II} \cdot \frac{D_m \Delta t \rho_{CO_2} RT}{d_0 M_{CO_2}}, C_0 = \frac{12 d_1^2 L \mu D_m}{\alpha h_0^4}, \varepsilon = \frac{\delta x h_0}{d_1 L} \tag{9b}$$

where M_{CO_2} is the molar mass of CO_2; ρ_{CO_2} is the density of CO_2; β is the capillary coefficient; σ is the interfacial tension; R is the ideal gas constant; T denotes the temperature; α is an attenuation factor that accounts for the wall roughness, friction or other flow rate loss effects. This attenuation factor α is the only parameter that needs to be calibrated in the theoretical model. Here, α is first calibrated as 0.004 using the experimental data at pH = 1 (Figure 4a) and then is used to predict the dissolution regimes for pH = 2, 3, and 4. As shown in Figures 4b–4d, the model prediction agrees very well with the experiments, indicating that the calibrated value of α is reasonable.

The theoretical model (Equation 9a and 9b) provides a generality extension of the regime boundary as a function of geometry (λ), capillarity (σ), and reactivity (Ψ or k). We validate this theoretical model using experimental patterns under various pH conditions (Figure 4 and Figure S10 in Supporting Information S1). All the parameters are kept the same as those used for the experiments are listed in the Table S2 in Supporting Information S1. As shown in Figure 4, the regime boundary predicted by the model agrees very well with the experimental results across different pH experiments. The model accurately depicts the shift in regimes from high reactivity to low reactivity. Furthermore, as the pH increases (from high to low reactivity), the classic dissolution regime (regime I) expands in area. This expansion correlates with observable physical phenomena and suggests that as reactivity diminishes, the regime toward a uniform pattern, thereby reinforcing the applicability of the classic surface-volume law. In summary, Equation 9a and 9b provides a generalized boundary for the dissolution regimes across various dissolution scenarios. It also provides a theoretical method to identify the predictability of the classic surface-volume law in a multiphase flow environment.

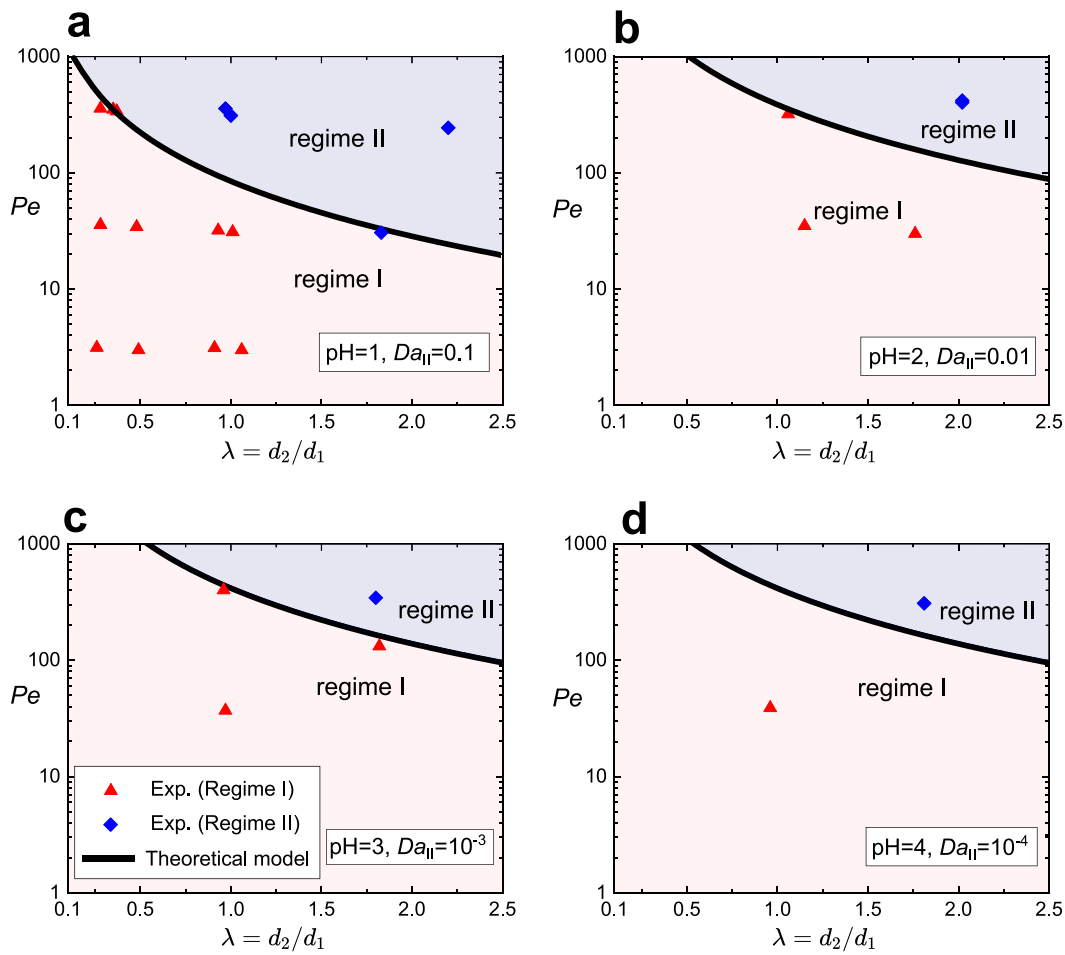

Figure 4. The theoretical model for the transition of the dissolution regimes in a multiphase flow environment. From the comparison between the predicted regime boundaries (solid line) and the experimental results (squares and triangles) with pH = 1 (a), pH = 2 (b), pH = 3 (c), and pH = 4 (d), the theoretical model (Equation 9a and 9b) can well capture the transition of the regime transition affected by the geometry (λ) and reactivity (Ψ or k). The parameters used in the theoretical prediction are listed in Table S2 in Supporting Information S1.

4. Conclusions

We establish a fundamental connection between the regimes and surface-volume scaling laws. If the dissolution exhibits a uniform pattern (regime I), a long-term dissolution rate can be predicted. However, if the dissolution exhibits the localized regime (regime II), the scaling deviates significantly from the classic law. We identify a pore-scale *barrier* mechanism that suppresses the overall dissolution rate and leads to this deviation. We propose a theoretical model that provides a generalized boundary for the dissolution regimes, and it further provide a theoretical method to identify the predictability of the classic surface-volume law. This work improves our understanding of how dissolution regimes control the scaling laws and their applicability and predictability in a multiphase-flow environment. Our theoretical model is a significant contribution to using the surface-volume scaling laws in reactive transport modeling. It has practical implications for geologic carbon sequestration and acid stimulation in carbonate reservoirs. In such applications, it is crucial to accurately estimate the overall dissolution rate under multiphase flow conditions. The multiphase flow *barrier effect* in regime II (localized) would suppress the increase of permeability and thus reduce the CO_2 leakage risk and the gas/oil recovery. This *barrier effect* should be considered to improve the precision of the reactive flow modeling at the field scales.

Data Availability Statement

Details of experiments and the images of this paper can be found in Supporting Information S1, and the datasets associated with this work are available at https://doi.org/10.5281/zenodo.8093436.

Acknowledgments
This work was supported by the National Natural Science Foundation of China (52122905), the Basic Science Center Program for Multiphase Media Evolution in Hypergravity of the National Natural Science Foundation of China (51988101), the Fundamental Research Funds for the Central Universities (No. 2042023kfyq03) and the National Natural Science Foundation of China (51925906, 42272158).

References

Alarji, H., Alzahid, Y., & Regenauer-Lieb, K. (2022). Acid stimulation in carbonates: Microfluidics allows accurate measurement of acidic fluid reaction rates in carbonate rocks by quantifying the produced CO_2 gas. *Journal of Natural Gas Science and Engineering*, *99*, 104444. https://doi.org/10.1016/j.jngse.2022.104444

Al-Khulaifi, Y., Lin, Q., Blunt, M. J., & Bijeljic, B. (2019). Pore-scale dissolution by CO_2 saturated brine in a multimineral carbonate at reservoir conditions: Impact of physical and chemical heterogeneity. *Water Resources Research*, *55*(4), 3171–3193. https://doi.org/10.1029/2018wr024137

Beckingham, L. E., Mitnick, E. H., Steefel, C. I., Zhang, S., Voltolini, M., Swift, A. M., et al. (2016). Evaluation of mineral reactive surface area estimates for prediction of reactivity of a multi-mineral sediment. *Geochimica et Cosmochimica Acta*, *188*, 310–329. https://doi.org/10.1016/j.gca.2016.05.040

Beckingham, L. E., Steefel, C. I., Swift, A. M., Voltolini, M., Yang, L., Anovitz, L. M., et al. (2017). Evaluation of accessible mineral surface areas for improved prediction of mineral reaction rates in porous media. *Geochimica et Cosmochimica Acta*, *205*, 31–49. https://doi.org/10.1016/j.gca.2017.02.006

Celia, M. A. (2017). Geological storage of captured carbon dioxide as a large-scale carbon mitigation option. *Water Resources Research*, *53*(5), 3527–3533. https://doi.org/10.1002/2017WR020841

Deng, H., Fitts, J. P., Tappero, R. V., Kim, J. J., & Peters, C. A. (2020). Acid erosion of carbonate fractures and accessibility of arsenic-bearing minerals: In operando synchrotron-based microfluidic experiment. *Environmental Science & Technology*, *54*(19), 12502–12510. https://doi.org/10.1021/acs.est.0c03736

Deng, H., Molins, S., Trebotich, D., Steefel, C., & DePaolo, D. (2018). Pore-scale numerical investigation of the impacts of surface roughness: Upscaling of reaction rates in rough fractures. *Geochimica et Cosmochimica Acta*, *239*, 374–389. https://doi.org/10.1016/j.gca.2018.08.005

Esteves, B. F., Spielman-Sun, E., Li, Q., Jew, A. D., Bargar, J. R., & Druhan, J. L. (2022). Geochemical modeling of celestite ($SrSO_4$) precipitation and reactive transport in shales. *Environmental Science & Technology*, *56*(7), 4336–4344. https://doi.org/10.1021/acs.est.1c07717

Fitts, J. P., & Peters, C. A. (2013). Caprock fracture dissolution and CO_2 leakage. *Reviews in Mineralogy and Geochemistry*, *77*(1), 459–479. https://doi.org/10.2138/rmg.2013.77.13

Hanna, R. B., & Rajaram, H. (1998). Influence of aperture variability on dissolutional growth of fissures in Karst Formations. *Water Resources Research*, *34*(11), 2843–2853. https://doi.org/10.1029/98wr01528

Holocher, J., Peeters, F., Aeschbach-Hertig, W., Kinzelbach, W., & Kipfer, R. (2003). Kinetic model of gas bubble dissolution in groundwater and its implications for the dissolved gas composition. *Environmental Science & Technology*, *37*(7), 1337–1343. https://doi.org/10.1021/es025712z

Hu, R., Li, K., Zhou, C., Wang, T., Yang, Z., & Chen, Y. (2023). On the role of gravity in dissolving horizontal fractures. *Journal of Geophysical Research: Solid Earth*, *128*(3), e2022JB025214. https://doi.org/10.1029/2022JB025214

Hu, R., Wan, J., Yang, Z., Chen, Y., & Tokunaga, T. (2018). Wettability and flow rate impacts on immiscible displacement: A theoretical model. *Geophysical Research Letters*, *45*(7), 3077–3086. https://doi.org/10.1002/2017GL076600

Hu, R., Wang, T., Yang, Z., Xiao, Y., Chen, Y.-F., & Zhou, C.-B. (2021). Dissolution hotspots in fractures. *Geophysical Research Letters*, *48*(20), e2021GL094118. https://doi.org/10.1029/2021GL094118

Hu, R., Zhou, C., Wu, D., Yang, Z., & Chen, Y. (2019). Roughness control on multiphase flow in rock fractures. *Geophysical Research Letters*, *46*(21), 12002–12011. https://doi.org/10.1029/2019GL084762

Hyman, J. D., Navarre-Sitchler, A., Andrews, E., Sweeney, M. R., Karra, S., Carey, J. W., & Viswanathan, H. S. (2022). A geo-structurally based correction factor for apparent dissolution rates in fractured media. *Geophysical Research Letters*, *49*(15), e2022GL099513. https://doi.org/10.1029/2022GL099513

Jiménez-Martínez, J., Hyman, J. D., Chen, Y., Carey, J. W., Porter, M. L., Kang, Q., et al. (2020). Homogenization of dissolution and enhanced precipitation induced by bubbles in multiphase flow systems. *Geophysical Research Letters*, *47*(7), e2020GL087163. https://doi.org/10.1029/2020gl087163

Kiani, S., Jafari, S., Apourvari, S. N., & Mehrjoo, H. (2021). Simulation study of wormhole formation and propagation during matrix acidizing of carbonate reservoirs using a novel in-situ generated hydrochloric acid. *Advances in Geo-Energy Research*, *5*(1), 64–74. https://doi.org/10.46690/ager.2021.01.07

Lasaga, A. C. (1984). Chemical kinetics of water-rock interactions. *Journal of Geophysical Research*, *89*(B6), 4009–4025. https://doi.org/10.1029/JB089iB06p04009

Le Traon, C., Aquino, T., Bouchez, C., Maher, K., & Le Borgne, T. (2021). Effective kinetics driven by dynamic concentration gradients under coupled transport and reaction. *Geochimica et Cosmochimica Acta*, *306*, 189–209. https://doi.org/10.1016/j.gca.2021.04.033

Li, L., Steefel, C. I., & Yang, L. (2008). Scale dependence of mineral dissolution rates within single pores and fractures. *Geochimica et Cosmochimica Acta*, *72*(2), 360–377. https://doi.org/10.1016/j.gca.2007.10.027

Li, P., Deng, H., & Molins, S. (2022). The effect of pore-scale two-phase flow on mineral reaction rates. *Frontiers in Water*, *3*, 734518. https://doi.org/10.3389/frwa.2021.734518

Ling, B., Sodwatana, M., Kohli, A., Ross, C. M., Jew, A., Kovscek, A. R., & Battiato, I. (2022). Probing multiscale dissolution dynamics in natural rocks through microfluidics and compositional analysis. *Proceedings of the National Academy of Sciences*, *119*(32), e2122520119. https://doi.org/10.1073/pnas.2122520119

Liu, M., Kwon, B., & Kang, P. K. (2022). Machine learning to predict effective reaction rates in 3D porous media from pore structural features. *Scientific Reports*, *12*(1), 5486. https://doi.org/10.1038/s41598-022-09495-0

Middleton, R. S., Gupta, R., Hyman, J. D., & Viswanathan, H. S. (2017). The shale gas revolution: Barriers, sustainability, and emerging opportunities. *Applied Energy*, *199*, 88–95. https://doi.org/10.1016/j.apenergy.2017.04.034

Molins, S., Soulaine, C., Prasianakis, N. I., Abbasi, A., Poncet, P., Ladd, A. J. C., et al. (2021). Simulation of mineral dissolution at the pore scale with evolving fluid-solid interfaces: Review of approaches and benchmark problem set. *Computational Geosciences*, *25*(4), 1285–1318. https://doi.org/10.1007/s10596-019-09903-x

Noiriel, C., & Daval, D. (2017). Pore-scale geochemical reactivity associated with CO_2 storage: New frontiers at the fluid–solid interface. *Accounts of Chemical Research*, *50*(4), 759–768. https://doi.org/10.1021/acs.accounts.7b00019

Noiriel, C., Madé, B., & Gouze, P. (2007). Impact of coating development on the hydraulic and transport properties in argillaceous limestone fracture. *Water Resources Research*, *43*(9), W09406. https://doi.org/10.1029/2006wr005379

Noiriel, C., & Soulaine, C. (2021). Pore-scale imaging and modelling of reactive flow in evolving porous media: Tracking the dynamics of the fluid–rock interface. *Transport in Porous Media*, *140*(1), 181–213. https://doi.org/10.1007/s11242-021-01613-2

Ott, H., & Oedai, S. (2015). Wormhole formation and compact dissolution in single- and two-phase CO_2-brine injections. *Geophysical Research Letters*, *42*(7), 2270–2276. https://doi.org/10.1002/2015gl063582

Panga, M. K. R., Ziauddin, M., & Balakotaiah, V. (2005). Two-scale continuum model for simulation of wormholes in carbonate acidization. *AIChE Journal*, *51*(12), 3231–3248. https://doi.org/10.1002/aic.10574

Qin, F., & Beckingham, L. E. (2021). The impact of mineral reactive surface area variation on simulated mineral reactions and reaction rates. *Applied Geochemistry*, *124*, 104852. https://doi.org/10.1016/j.apgeochem.2020.104852

Roded, R., Aharonov, E., Holtzman, R., & Szymczak, P. (2020). Reactive flow and homogenization in anisotropic media. *Water Resources Research*, *56*(12), e2020WR027518. https://doi.org/10.1029/2020wr027518

Roded, R., Szymczak, P., & Holtzman, R. (2021). Wormholing in anisotropic media: Pore-scale effect on large-scale patterns. *Geophysical Research Letters*, *48*(11), e2021GL093659. https://doi.org/10.1029/2021GL093659

Romanov, D., Gabrovšek, F., & Dreybrodt, W. (2003). Dam sites in soluble rocks: A model of increasing leakage by dissolutional widening of fractures beneath a dam. *Engineering Geology*, *70*(1–2), 17–35. https://doi.org/10.1016/s0013-7952(03)00073-5

Seigneur, N., Mayer, K. U., & Steefel, C. I. (2019). Reactive transport in evolving porous media. *Reviews in Mineralogy and Geochemistry*, *85*(1), 197–238. https://doi.org/10.2138/rmg.2019.85.7

Song, W., Ogunbanwo, F., Steinsbø, M., Fernø, M. A., & Kovscek, A. R. (2018). Mechanisms of multiphase reactive flow using biogenically calcite-functionalized micromodels. *Lab on a Chip*, *18*(24), 3881–3891. https://doi.org/10.1039/c8lc00793d

Soulaine, C., Roman, S., Kovscek, A., & Tchelepi, H. A. (2018). Pore-scale modelling of multiphase reactive flow: Application to mineral dissolution with production of CO_2. *Journal of Fluid Mechanics*, *855*, 616–645. https://doi.org/10.1017/jfm.2018.655

Steefel, C. I., Appelo, C. A. J., Arora, B., Jacques, D., Kalbacher, T., Kolditz, O., et al. (2015). Reactive transport codes for subsurface environmental simulation. *Computational Geosciences*, *19*(3), 445–478. https://doi.org/10.1007/s10596-014-9443-x

Steefel, C. I., & Lichtner, P. C. (1998). Multicomponent reactive transport in discrete fractures II: Infiltration of hyperalkaline groundwater at Maqarin, Jordan, a natural analogue site. *Journal of Hydrology*, *25*, 200–224.

Steefel, C. I., & Maher, K. (2009). Fluid-rock interaction: A reactive transport approach. *Reviews in Mineralogy and Geochemistry*, *70*(1), 485–532. https://doi.org/10.2138/rmg.2009.70.11

Steefel, C. I., Molins, S., & Trebotich, D. (2013). Pore scale processes associated with subsurface CO_2 injection and sequestration. *Reviews in Mineralogy and Geochemistry*, *77*(1), 259–303. https://doi.org/10.2138/rmg.2013.77.8

Thompson, K. E., & Gdanskl, R. D. (1993). Laboratory study provides guidelines for diverting acid with foam. *SPE Production and Facilities*, *8*(04), 285–290. https://doi.org/10.2118/23436-PA

Wang, C., Li, W., Yang, Z., Chen, Y., Shao, W., & Ji, J. (2015). An invisible soil acidification: Critical role of soil carbonate and its impact on heavy metal bioavailability. *Scientific Reports*, *5*(1), 12735. https://doi.org/10.1038/srep12735

Wang, T., Hu, R., Yang, Z., Zhou, C.-X., Chen, Y.-F., & Zhou, C.-B. (2022). Transitions of dissolution patterns in rough fractures. *Water Resources Research*, *58*(1), e2021WR030456. https://doi.org/10.1029/2021WR030456

Wen, H., & Li, L. (2017). An upscaled rate law for magnesite dissolution in heterogeneous porous media. *Geochimica et Cosmochimica Acta*, *210*, 289–305. https://doi.org/10.1016/j.gca.2017.04.019

Xu, J., & Balhoff, M. T. (2022). Dissolution-after-precipitation (DAP): A simple microfluidic approach for studying carbonate rock dissolution and multiphase reactive transport mechanisms. *Lab on a Chip*, *22*(21), 4205–4223. https://doi.org/10.1039/D2LC00426G

Xu, T., Tian, H., Zhu, H., & Cai, J. (2022). China actively promotes CO_2 capture, utilization and storage research to achieve carbon peak and carbon neutrality. *Advances in Geo-Energy Research*, *6*(1), 1–3. https://doi.org/10.46690/ager.2022.01.01

Yoon, H., Valocchi, A. J., Werth, C. J., & Dewers, T. (2012). Pore-scale simulation of mixing-induced calcium carbonate precipitation and dissolution in a microfluidic pore network. *Water Resources Research*, *48*(2), 103885. https://doi.org/10.1029/2011wr011192

Yortsos, Y. C., & Stubos, A. K. (2001). Phase change in porous media. *Interface Science*, *6*(3), 208–216. https://doi.org/10.1016/s1359-0294(01)00085-1

Yu, Y., Wang, C., Liu, J., Mao, S., Mehmani, Y., & Xu, K. (2023). Bubble coarsening kinetics in porous media. *Geophysical Research Letters*, *50*(1), e2022GL100757. https://doi.org/10.1029/2022GL100757

Zhang, L., Chen, L., Hu, R., & Cai, J. (2022). Subsurface multiphase reactive flow in geologic CO_2 storage: Key impact factors and characterization approaches. *Advances in Geo-Energy Research*, *6*(3), 179–180. https://doi.org/10.46690/ager.2022.03.01

Zhang, Y., Jiang, F., & Tsuji, T. (2022). Influence of pore space heterogeneity on mineral dissolution and permeability evolution investigated using lattice Boltzmann method. *Chemical Engineering Science*, *247*, 117048. https://doi.org/10.1016/j.ces.2021.117048

Zhou, C.-X., Hu, R., Li, H.-W., Yang, Z., & Chen, Y.-F. (2022). Pore-scale visualization and quantification of dissolution in microfluidic rough channels. *Water Resources Research*, *58*(11), e2022WR032255. https://doi.org/10.1029/2022WR032255

Zuo, L., Zhang, C., Falta, R. W., & Benson, S. M. (2013). Micromodel investigations of CO_2 exsolution from carbonated water in sedimentary rocks. *Advances in Water Resources*, *53*, 188–197. https://doi.org/10.1016/j.advwatres.2012.11.004